Thin Solid Films 782 (2023) 139968

Contents lists available at ScienceDirect

Thin Solid Films

journal homepage: www.elsevier.com/locate/tsf

Characteristics of ZnON films and heterojunction diodes with varying O:N ratios

Kjetil Karlsen Saxegaard *, Eduard Monakhov, Lasse Vines, Kristin Bergum

Department of Physics/Centre for Materials Science and Nanotechnology, University of Oslo, N-0316 Oslo, Norway

ARTICLE INFO

Keywords:
Zinc oxynitride
Diode
Band gap
Mobility
Electron concentration
Current–voltage
Capacitance–voltage

ABSTRACT

Zinc Oxynitride (ZnO_xN_y) thin films display high mobilities and a considerable tunability of both the free electron concentration and optical band gap. The properties achievable for this material system makes ZnO_xN_y an intriguing n-type absorber candidate in silicon-based tandem solar cells. We have studied how the O:N ratio affect structural, optical and electrical properties of magnetron sputtered ZnO_xN_y thin films, as well the electrical behavior of ZnO_xN_y-Si pn heterojunction diodes. X-ray diffraction of the ZnO_xN_y films indicate either a Zn_3N_2-like structure or ZnO-like grains in combination with structural disorder. As the O:N ratio is increased, the optical band gap of ZnO_xN_y films increase from 1.1 to 1.9 eV. Hall effect measurements of the n-type ZnO_xN_y films show free electron concentrations varying with the O:N ratio, from 9.8×10^{17} to 1.5×10^{16} cm^{-3}. Hall mobility up to 88 cm^2/Vs is achieved. We observe the formation of pn heterojunction diodes between ZnO_xN_y-films and p-Si. The electrical characteristics of these diodes are shown to depend on the ZnO_xN_y anion composition. Current rectification of 3.7 orders of magnitude is achieved between -1 and 1 V at room temperature. However, the built in voltage extracted from capacitance–voltage measurements are higher than theory suggest, implying an influence of defects on the electrical characteristics.

1. Introduction

Zinc oxynitride (ZnO_xN_y) is a n-type semiconductor that has gained recent attention due to its potential as a high mobility gate in thin-film-transistors. Both electrical and optical properties are easily tunable within a range that enables other potential applications, such as tandem solar cells, photodetectors, etc. Importantly, films can be deposited by magnetron sputtering at low temperatures, making it suitable for large scale manufacturing.

The electrical conduction of ZnO_xN_y films are significantly affected by the O:N ratio. Hall mobilities up to 120 cm^2/Vs [1–4] has been achieved for nitrogen-rich, magnetron sputtered films. Free electron concentration is observed to decrease as the O:N ratio increases, with reported values ranging from 10^{16} to 10^{20} cm^{-3} [5,6]. Notably, these values are observed despite highly disordered crystal structures or even amorphous films.

In addition, the O:N ratio strongly influence the optical band gap of ZnO_xN_y films, shown to vary from 1.1 to 3.2 eV [7–10]. This range is ideal for the optimization of a top cell absorber in a monolithic, two terminal tandem solar cell with a Si-bottom cell. With a top cell absorber band gap of $\sim$ 1.7 eV, the theoretical efficiency increases with near 50% compared to a Si-only solar cell [11]. However, little research has been performed on the electrical properties of ZnO_xN_y films and diodes with or in the vicinity of this band gap.

The few demonstrated diodes with ZnO_xN_y exhibit current rectification of approximately three orders of magnitude between −1 and 1 V, achieved with a zinc–cobalt oxide/ZnO_xN_y pn heterojunction [12] and a Ni/Al_2O_3/ZnO_xN_y metal–insulator diode [13]. However, these reports do not elaborate on how anion composition or deposition parameters influence diode behavior.

This work aim to elucidate on how the anion composition influence ZnO_xN_y films and ZnO_xN_y–silicon heterojunction diodes deposited by magnetron sputtering. RF and DC sputtered films and diodes are also compared. Specifically, current–voltage and capacitance–voltage of heterojunction diodes are analyzed in light of the structural, electrical and optical properties of ZnO_xN_y films.

2. Experimental details

2.1. Deposition and sample preparation

ZnO_xN_y films were grown in a Polyteknik Flextura magnetron sputtering system at room temperature, with a chamber base pressure

* Corresponding author.
E-mail address: k.k.saxegaard@mn.uio.no (K.K. Saxegaard).

https://doi.org/10.1016/j.tsf.2023.139968
Received 2 January 2023; Received in revised form 17 May 2023; Accepted 1 July 2023
Available online 11 July 2023
0040-6090/© 2023 The Author(s). Published by Elsevier B.V. This is an open access article under the CC BY license (http://creativecommons.org/licenses/by/4.0/).

< 2×10^{-6} Pa. A 3" Zn target (99.995%) was subjected to either 150 W RF (19.7 W/cm^2) or 100 W DC (13.1 W/cm^2) power in a 1 Pa atmosphere consisting of O_2, N_2 and Ar. The flow of O_2 and N_2 were varied, but the sum of O_2 and N_2 flow was kept constant at 20 sccm. Specific deposition parameters for the films in this work are summarized in Table 1.

Films were deposited simultaneously on both Fused Silica (FS) and Boron-doped (100), Czochralski Si substrates. The p-Si substrate had a resistivity of 7.5 Ωcm, as measured by a Jandel KM3-AR 4-point probe. This corresponds to a doping of 1.8×10^{15} cm^{-3}. In order to avoid oxidation of the films, samples were stored in a N_2 filled glove box [14,15].

The ZnO_xN_y–Si heterojunction diodes were prepared by depositing 300 nm Al Ohmic front contacts in an Angstrom EvoVac e-beam system. Depositions were performed with a rate of 0.05 nm/s at room temperature, from a base pressure < 10^{-4} Pa. Mesa diodes were defined by placing droplets of Microposit 1813 photo resist on the Al-contacts, drying in room temperature and then etching in 1:100 HCl:deionized water. Silver paste was used for the Ohmic contact on the back side of the Si-substrate.

2.2. Characterization

Film thickness was evaluated by a Veeco Dektak 8 Stylus Profilometer on films with sharp edges defined by etching. Composition was analyzed with SEM-based Energy Dispersive X-ray Spectroscopy (EDS), using a JEOL IT-300 equipped with a ThermoScientific Ultradry detector and Pathfinder X-ray microanalysis software. EDS measurements with a 20 kV acceleration voltage revealed Zn, O and N as major constituents, in addition unavoidable surface carbon. However, trace amounts of Fe Kα was also observed. Stoichiometry was calculated from a 3 kV spectra, in order to reduce X-ray intensity decay for light elements [16] and a standardless phi–rho–Z analysis. All spectra were acquired using a count-rate of 6400 ns and 20% dead time. An acceleration voltage of 3 kV correspond to 95% of all characteristic X-rays being generated within 41 nm from the surface, as calculated by *Casino v2.5* [17] and an assumed film density of 6.4 g/cm^3.

Structural analysis is based on X-ray Diffraction (XRD) 2θ measurements of films on Si substrates. A Bruker AXS D8 Discover system with a Cu Kα ($\lambda = 0.15406$ nm) X-ray source was used, equipped with a Ge (220) double bounce monochromator filtering out Kα_2 ($\lambda = 0.15444$ nm) signals. A step size of $\Delta 2\theta = 0.01°$ was used.

Optical transmission and reflection measurements of fused-silica grown samples were performed at room temperature using a Shimadzu SolidSpec-3700 DUV with an integrating sphere.

Room temperature Hall measurements were conducted on films grown on FS substrates. A LakeShore 7604 with 1.3 T magnetic field was used to measure RF3 and DC1, due to high resistivity. A homemade setup with Keithley 7001, 2182 A and 6221 and a 1.02 T magnet were used for samples with Hall mobility > 25 cm^2/Vs (RF1 and RF2). Diodes were characterized by Current–Voltage (IV) and frequency dependent Capacitance–Voltage (CV) measurements, using a Keithley 8410 and an Agilent 4280 A LCR-meter respectively.

3. Results

3.1. Composition and crystal structure

SEM-EDS reveal emission from O–Kα, N–Kα and Zn–L peaks, in addition to unavoidable C–Kα on the surface, as shown in the 3 kV spectra in Fig. 1. The concentration of oxygen increase from 8.6 at.% in RF1 to 32.7 at.% in RF3, normalized by the sum of Zn, O, and N. All films has a Zn concentration of ∼ 50%. Therefore, the O:N ratio is significantly increased by increasing the O_2 flow during deposition as summarized in Table 1. Unfortunately, EDS does not distinguish between different local chemical environments. The degree to which oxygen and nitrogen can exist in interstitial or substitutional positions, as molecular species or other bonding configurations is not possible to determine.

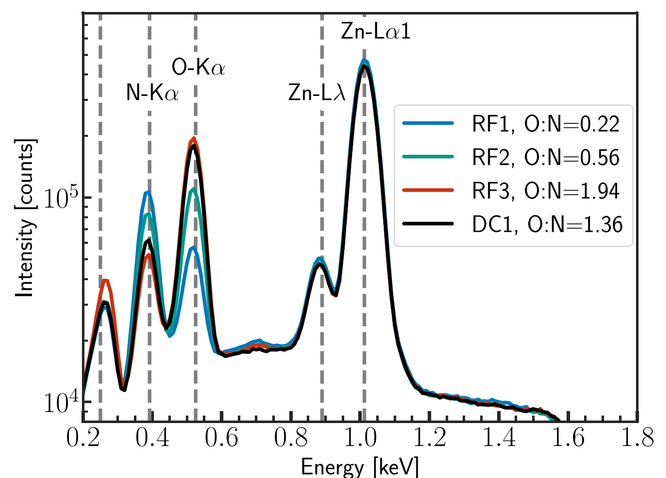

Fig. 1. EDS spectra for the different films, acquired with a 3 kV accelerating voltage.

Table 1
Summary of the deposition parameters explored in this work, together with film thickness obtained by profilometry and oxygen concentration and O:N ratio of films derived from EDS.

Film	Deposition details		Film properties		
	Target power	$\frac{O_2}{O_2+N_2}$	Thickness	[O]	O:N
RF1	150 W RF	2%	1030 ± 10 nm	$8.6\pm0.2\%$	0.22
RF2	150 W RF	3%	1040 ± 10 nm	$18.1\pm0.3\%$	0.56
RF3	150 W RF	4.5%	1250 ± 10 nm	$32.7\pm0.6\%$	1.94
DC1	100 W DC	11%	960 ± 20 nm	$29.6\pm0.6\%$	1.36

An additional feature, barely discernible over the bremsstrahlung background, can be seen around 0.7 keV in Fig. 1. This coincides with Fe–Lα radiation, expected from the observation of Fe–Kα peaks in the 20 kV spectra described in Section 2.2. Attempts at estimating such small features is challenging, but the Fe-concentration is < 0.2 at.% in all films.

Distinct XRD diffraction patterns are observed in every film. As shown in Fig. 2, the sole peak in the nitrogen rich RF1 film at $2\Theta = 53.2°$ is related to cubic Zn_3N_2 (440). This peak has previously been observed for ZnO_xN_y-films [18]. The small mismatch between the powder-based database value of Zn_3N_2 (440) [19] and our films is attributed to thin film strain and oxygen incorporation. The more oxygen rich RF2 have a singular peak in the vicinity of Zn_3N_2 (440), but shifted towards a higher 2θ-value. Therefore, the diffraction peak for RF2 is assigned to a Zn_3N_2 (440) like plane in ZnO_xN_y, but with a 2.5% reduction in the lattice constant compared to the powder-based database value for Zn_3N_2. A similar effect has been observed previously by Gao et al. [20].

The oxygen rich samples RF3 and DC1 have decidedly different diffractograms compared to the two oxygen poor samples RF1 and RF2. Both have a single peak between 32–33°. This is attributed to severely strained ZnO (002), previously observed for ZnO_xN_y films [4,7,20–22]. However, this interpretation corresponds to a c-axis constant increase over the database-values [23] of 3.6% and 7.2% for RF3 and DC1 respectively. In addition, these two oxygen rich samples have a broad feature between 35 and 40°. This feature is not related to a known crystal plane. Due to the non-equilibrium growth conditions, we attribute this feature to highly disordered grains, potentially metastable and nanometer-sized [4,24]. Note that ZnO (101), Zn_3N_2 (400) and (411) diffraction values are all within the range of the feature.

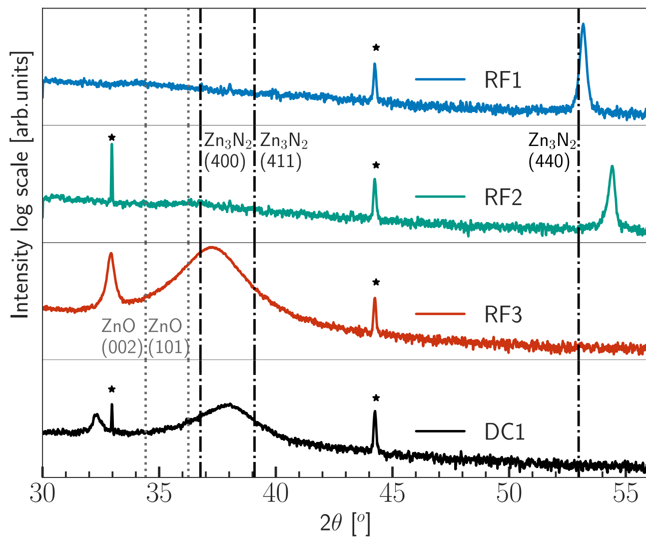

Fig. 2. XRD diffractograms of samples grown on Si-substrates. The asterisk indicate peaks not related to the ZnO_xN_y film. The asterix at 32.89° is a forbidden (200) Si peak with a ϕ dependent intensity, whereas the peak at 44.5° is from the sample holder. Dotted lines refer to database values of theoretical calculations of Zn_3N_2 [19] and experimental ZnO measurements [23].

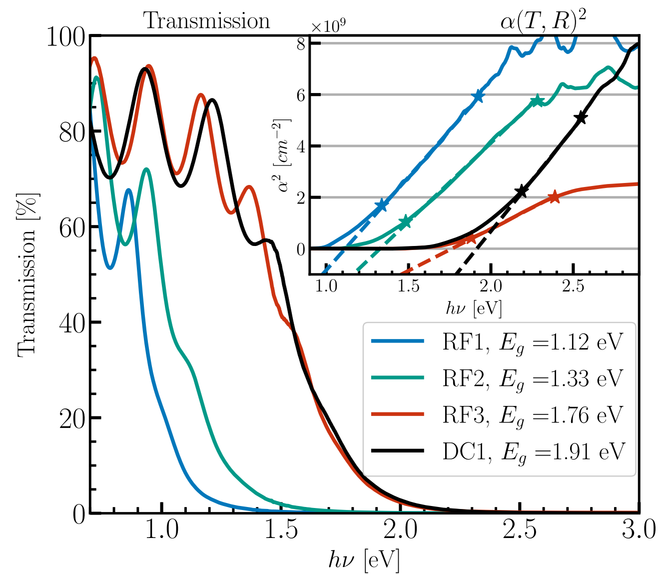

Fig. 3. Optical transmission of films as a function of photon energy. Inset shows $\alpha^2(h\nu)$, where asterisks indicate the start and end points of linear regression.

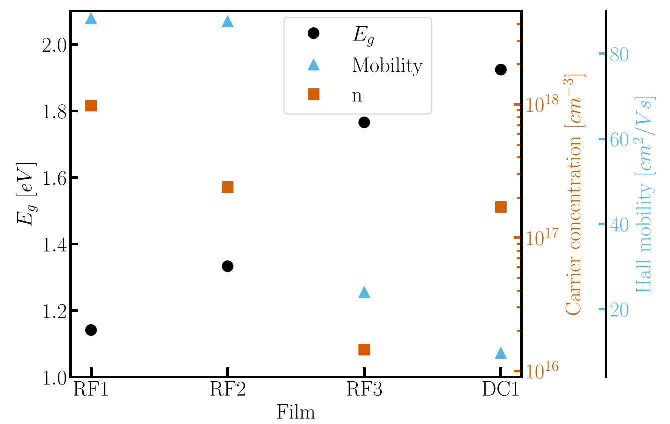

Fig. 4. Free carrier concentration, Hall mobility and optical band gap at room temperature.

3.2. Optical band gap

The optical transmission of films at photon energies lower than the absorption edge energy is characterized by constructive interference in the films, seen as fringes in Fig. 3. Further, we observe an increase in the apparent absorption onset as the O:N ratio increase, from between 1.0–1.3 eV for RF1 to between 1.6–2.1 eV for RF3. An accurate description of the absorption edge energy requires a precise description of the absorption coefficient α, achieved by combining transmission and reflection measurements [25].

Estimating the optical band gap by the commonly utilized Tauc-analysis yielded ambiguous and nonphysical conclusions. A pronounced linear dependence could not be found when plotting $(\alpha h\nu)^\gamma$ as a function of $h\nu$ for direct allowed transitions ($\gamma = 2$). Although some linear dependencies were observed for indirect transitions ($\gamma = 0.5$), the extracted absorption edge energies were significantly lower than the rough onset estimates discussed above. Note that a fundamental assumptions of Tauc-analysis is an amorphous structure, where momentum does not need to be conserved and the conduction band is described by localized states [25–28]. An alternative approach were therefore chosen, consistent with crystalline structures [25,26,29–31]. Similar to Tauc analysis, the model predicts a linear dependency on $h\nu$ near the absorption edge and is presented in Eq. (1).

$$\alpha^\gamma \propto (h\nu - E_G), \qquad \text{for} \quad h\nu \geq E_G \tag{1}$$

The absorption edges of all films are best described by direct allowed transitions, i.e. $\gamma = 2$, as shown in the inset of Fig. 3. Estimates of the optical band gap are based on linear regression near the absorption edge, with a required goodness-of-fit parameter $R^2 \geq 0.999$ over a $h\nu$ region larger than 0.3 eV. It is confirmed that increasing the oxygen concentration in the RF-series yields a higher absorption edge energy, from $E_G = 1.12$ to $E_G = 1.76$ eV in RF1 and RF3 respectively. The band gap of RF3 is suitable for a top cell absorber in two-terminal tandem solar cells which utilizes a silicon bottom cell. Despite a lower O:N ratio than RF3, DC1 has the highest absorption edge energy. This implies a difference in chemical environment of nitrogen between RF3 and DC1. Considering the higher target power of RF3 over DC1, one can speculate that DC1 has a higher degree of molecular nitrogen (N_2) than RF3.

3.2.1. Hall effect

Hall effect measurements confirm n-type conductivity in all films. The free electron concentration, shown in Fig. 4, decreases by nearly two orders of magnitude as the O:N ratio increases, from 9.8×10^{17} to 1.5×10^{16} cm^{-3} for RF1 and RF3 respectively. DC1's free carrier concentration is an order of magnitude larger than that of RF3, despite an absorption edge energy comparable to RF3.

Both the oxygen-poor samples RF1 and RF2 have a Hall mobility of 88 cm^2/Vs. Further increases in the O:N ratio of films results in a notable decline in mobility. Interestingly, this decrease coincide with structural changes observed by XRD. Both of the oxygen rich samples RF3 and DC1 have a different crystallographic structure and larger degree of structural disorder than RF1 and RF2. This trend contrast some reports on ZnO_xN_y-films, where disorder is considered advantageous for high mobility [4,5,32]. However, more extensive measurements are required to describe the physical processes determining or limiting the electron mobility.

3.3. Current–voltage of diodes

The mesa diodes consisting of ZnO_xN_y deposited on moderately doped p-Si substrates yielded rectifying junctions for all O:N ratios.

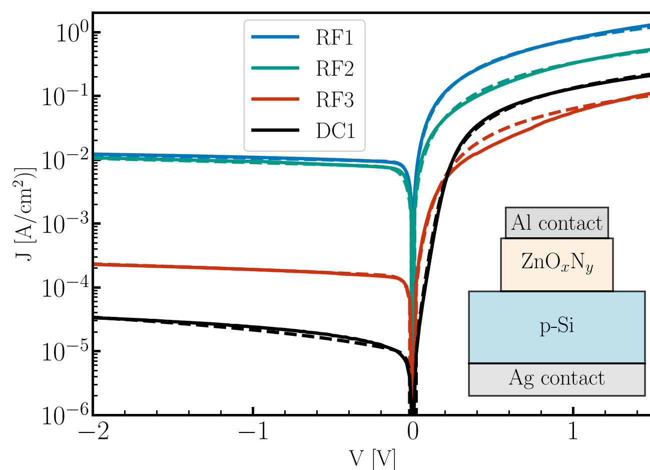

Fig. 5. Current density as a function of voltage. The dashed lines is the result of fitting the JV-curve to Eq. (2). The mesa-diode illustration is not to scale.

Table 2
Reverse current, ideality factor, series and shunt resistance necessary for fitting the JV measurements to Eq. (2).

Diode	J_0 [A/cm²]	R_{sh} [Ω]	n	R_S [Ω]
RF1	$(4.4 \pm 0.2) \times 10^{-5}$	$(1.5 \pm 0.2) \times 10^{5}$	1.2 ± 0.2	$(2.0 \pm 0.1) \times 10^{2}$
RF2	$(6.2 \pm 0.3) \times 10^{-5}$	$(8.5 \pm 2) \times 10^{4}$	1.8 ± 0.3	$(3.2 \pm 0.1) \times 10^{2}$
RF3	$(1.3 \pm 0.2) \times 10^{-6}$	$(2.6 \pm 0.6) \times 10^{6}$	1.5 ± 0.2	$(1.3 \pm 0.1) \times 10^{3}$
DC1	$(8 \pm 0.4) \times 10^{-8}$	$(1.0 \pm 0.1) \times 10^{7}$	1.1 ± 0.05	$(6.6 \pm 0.4) \times 10^{2}$

However, only DC1 has a pronounced exponential region, which results in an ideality factor n of 1.1 when fitted to Eq. (2). This extended diode equation expands the ideal diode equation with a series resistance R_S and a parallel shunt resistance R_{sh} [33]. All diodes have been fitted to this equation, with various success as shown in Fig. 5 and Table 2. Further, all diodes are limited by series resistance in forward bias.

$$I = I_s\left(e^{\frac{q(V-IR_s)}{nk_bT}} - 1\right) + \frac{V - IR_s}{R_{sh}} \tag{2}$$

The oxygen-poor RF deposited ZnO_xN_y diodes have high reverse current densities of $J_0 \sim 10^{-2}$ A/cm² and consequently low rectification. Increasing the O:N ratio to that of RF3 results in a significant decrease in J_0. However, the lowest J_0 is achieved with DC1, despite a lower O:N ratio than RF3. DC1 thus achieves the highest current rectification of 3.7 orders of magnitude between −1 and 1 V.

The trend in J_0 cannot be explained by simply considering the difference in free electron concentration, mobility and band gap as in the drift–diffusion approximation. On the other hand, the shift in J_0 coincide with the changes in crystal structure as observed by XRD. A change of the ZnO_xN_y structure could yield different defects dominating the electron transport. In addition, it would affect the interface between ZnO_xN_y and Si. A high degree of defect states, either in bulk ZnO_xN_y or at the ZnO_xN_y–Si interface is expected to influence the electric conduction through the hetereojunctions.

3.4. Capacitance–voltage

For ideal diodes, a plot of $C^{-2}(V)$ yield a linear slope. For the diodes in this study, this is true for $V < -1$ V when measuring with a 1 MHz probing frequency at room temperature, as shown in Fig. 6(a). The slopes of RF1, RF2 and DC1 corresponds to asymmetrical diodes, as the extracted ionized donor concentration from $C^{-2}(V)$ yields the Si-substrate doping. On the other hand, the steeper slope of RF3 corresponds to a more symmetric junction with a non-negligible depletion layer in the ZnO_xN_y. This result corresponds well with the independent calculations of the diode band structure shown in Fig. 6(b), which show a depletion region mostly in Si. These simulations are performed with Silvaco Atlas and are based on an assumed electron affinity of $\chi_{ZnON} = 4.6$ [2,10,34], the band gap and Hall results of RF3, in addition to no defect states and interface-layers.

Every diode deviate from a linear $C^{-2}(V)$ dependence at voltages between −0.1 and 0 V. However, RF3 yields non-linear dependence at the larger interval −1 to 0 V. As a consequence, all estimates of the apparent built-in Voltage V_0 is calculated from the region $V < -1$ V.

Apparent V_0 values are found to vary from 0.7 to 1.6 V at room temperature and 1 MHz probing frequency. The values are significantly higher than expected from the Anderson electron affinity rule, which predicts $V_0 \leq 0.29$ V for all diodes. Both the high V_0 and the non-linearity of $C^{-2}(V)$ are attributed to a presence of defects near or at the interface.

4. Summary

ZnO_xN_y films with varying anion composition were deposited using RF and DC magnetron sputtering. Crystalline films are formed, with a micro-structure highly dependent on the anion composition. Optical band gap increases with higher O:N ratios for RF-deposited films, up to 1.76 eV. On the other hand, free carrier concentration is reduced by near two orders of magnitude as the O:N ratio increase. Of particular interest for a PV tandem top cell absorber is the combination of $n = 1.5 \times 10^{16}$ cm^{-3} and $E_G = 1.76$ eV. ZnO_xN_y deposited on p-Si forms pn diodes, with a rectification up 3.7 orders of magnitude between −1 and 1 V. We observe indication of defects in these heterojunction diodes that affect the electrical characteristics of the junction, either in the ZnO_xN_y layer or at the interface between ZnO_xN_y and Si.

CRediT authorship contribution statement

Kjetil Karlsen Saxegaard: Conceptualization, Methodology, Formal analysis, Investigation, Writing – original draft, Writing – review & editing, Visualization. **Eduard Monakhov:** Conceptualization, Supervision, Writing – review & editing. **Lasse Vines:** Supervision, Writing – review & editing. **Kristin Bergum:** Conceptualization, Methodology, Validation, Project administration, Funding acquisition.

Declaration of competing interest

The authors declare the following financial interests/personal relationships which may be considered as potential competing interests: Kristin Bergum reports financial support was provided by Research Council of Norway.

Data availability

Data will be made available on request.

Acknowledgments

The Research Council of Norway is acknowledged for the support to the project *New MAterials for Tandem Solar cells*, project number 288596 and the Norwegian Micro- and Nano-Fabrication Facility, NorFab, project number 295864.

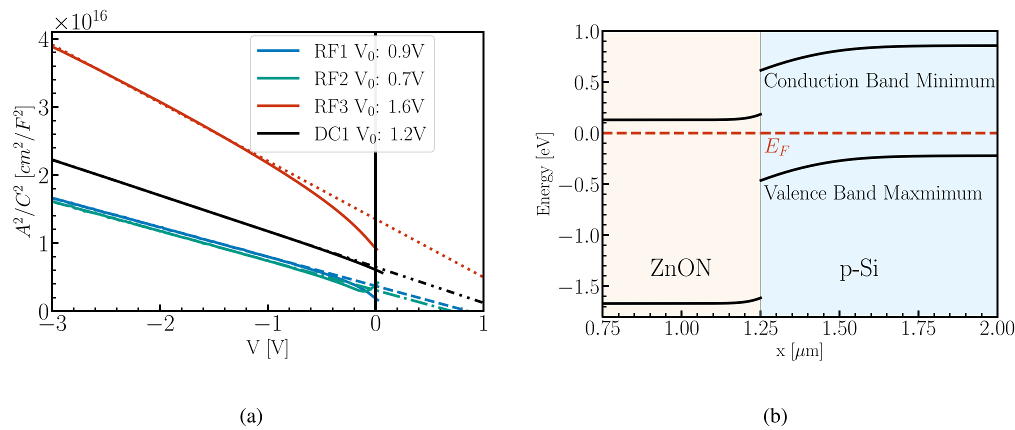

Fig. 6. Room temperature $C^{-2}(V)$ measured with a 1 MHz probing frequency (a), with linear regression of the region $V < -1$ V from which apparent V_0 is based (dashed lines). Expected band diagram of the RF3-diode assuming $\chi_{ZnON} = 4.6$ eV (b).

References

[1] E. Lee, T. Kim, A. Benayad, J. Hur, G.-S. Park, S. Jeon, High mobility and high stability glassy metal-oxynitride materials and devices, Sci. Rep. 6 (1) (2016) 23940, http://dx.doi.org/10.1038/srep23940.

[2] Myungkwan Ryu, Tae Sang Kim, Kyoung Seok Son, Hyun-Suk Kim, Joon Seok Park, Jong-Baek Seon, Seok-Jun Seo, Sun-Jae Kim, Eunha Lee, Hyungik Lee, Sang Ho Jeon, Seungwu Han, Sang Yoon Lee, High mobility zinc oxynitride-TFT with operation stability under light-illuminated bias-stress conditions for large area and high resolution display applications, in: 2012 International Electron Devices Meeting, vol. 717, IEEE, 2012, pp. 5.6.1–5.6.3, http://dx.doi.org/10.1109/IEDM.2012.6478986.

[3] Hyoung-Do Kim, Jong Heon Kim, Kyung Park, Jung Hyun Kim, Jozeph Park, Yong Joo Kim, Hyun-Suk Kim, Effects of fluorine doping on the electrical performance of ZnON thin-film transistors, ACS Appl. Mater. Interfaces 9 (29) (2017) 24688–24695, http://dx.doi.org/10.1021/acsami.7b03385.

[4] Eunha Lee, A. Benayad, T. Shin, H. Lee, D.-S. Ko, T.S. Kim, K.S. Son, M. Ryu, S. Jeon, G.-S. Park, Nanocrystalline ZnON; High mobility and low band gap semiconductor material for high performance switch transistor and image sensor application, Sci. Rep. 4 (1) (2014) 4948, http://dx.doi.org/10.1038/srep04948.

[5] Takanori Yamazaki, Kei Shigematsu, Yasushi Hirose, Shoichiro Nakao, Isao Harayama, Daiichiro Sekiba, Tetsuya Hasegawa, Amorphous ZnO x N y thin films with high electron hall mobility exceeding 200 cm2V-1s-1, Appl. Phys. Lett. 109 (26) (2016) 262101, http://dx.doi.org/10.1063/1.4973203.

[6] Y. Ye, R. Lim, J.M. White, High mobility amorphous zinc oxynitride semiconductor material for thin film transistors, J. Appl. Phys. 106 (7) (2009) 074512, http://dx.doi.org/10.1063/1.3236663.

[7] M. Futsuhara, K. Yoshioka, O. Takai, Optical properties of zinc oxynitride thin films, Thin Solid Films 317 (1–2) (1998) 322–325, http://dx.doi.org/10.1016/S0040-6090(97)00646-9.

[8] Jozeph Park, Hyun-Jun Jeong, Hyun-Mo Lee, Ho-Hyun Nahm, Jin-Seong Park, The resonant interaction between anions or vacancies in ZnON semiconductors and their effects on thin film device properties, Sci. Rep. 7 (1) (2017) 2111, http://dx.doi.org/10.1038/s41598-017-02336-5.

[9] Dae-Hwan Kim, Hwan-Seok Jeong, Chan-Yong Jeong, Sang-Hun Song, Hyuck-In Kwon, Effects of oxygen flow rate on the electrical stability of zinc oxynitride thin-film transistors, Japan. J. Appl. Phys. 56 (2) (2017) 020301, http://dx.doi.org/10.7567/JJAP.56.020301.

[10] Hyun-Suk Kim, Sang Ho Jeon, Joon Seok Park, Tae Sang Kim, Kyoung Seok Son, J.-B. Seon, S.-J. Seo, S.-J. Kim, E. Lee, J.G. Chung, H. Lee, S. Han, M. Ryu, S.Y. Lee, K. Kim, Anion control as a strategy to achieve high-mobility and high-stability oxide thin-film transistors, Sci. Rep. 3 (1) (2013) 1459, http://dx.doi.org/10.1038/srep01459.

[11] Sven Rühle, The detailed balance limit of perovskite/silicon and perovskite/CdTe tandem solar cells, Phys. Status Solidi a 214 (5) (2017) 1600955, http://dx.doi.org/10.1002/pssa.201600955.

[12] Anna Reinhardt, Holger von Wenckstern, Marius Grundmann, Metal–semiconductor field-effect transistors based on the amorphous multi-anion compound ZnON, Adv. Electron. Mater. 6 (4) (2020) 1901066, http://dx.doi.org/10.1002/aelm.201901066.

[13] Mohamad Hazwan Mohd Daut, John F. Wager, Arokia Nathan, ZnON MIS thin-film diodes, IEEE J. Electron Device. Soc. 7 (February) (2019) 375–381, http://dx.doi.org/10.1109/JEDS.2019.2900542.

[14] E. Lee, T. Kim, A. Benayad, H. Kim, S. Jeon, G.-S. Park, Ar plasma treated ZnON transistor for future thin film electronics, Appl. Phys. Lett. 107 (12) (2015) 122105, http://dx.doi.org/10.1063/1.4930827.

[15] T. Kim, M.J. Kim, J. Lee, J.K. Jeong, Boosting carrier mobility in zinc oxynitride thin-film transistors via tantalum oxide encapsulation, ACS Appl. Mater. Interfaces 11 (25) (2019) 22501–22509, http://dx.doi.org/10.1021/acsami.9b03865.

[16] Anwar Ul-Hamid, A beginners' guide to scanning electron microscopy, in: A Beginners' Guide To Scanning Electron Microscopy, first ed., Springer, 2018, http://dx.doi.org/10.1007/978-3-319-98482-7.

[17] Dominique Drouin, Alexandre Réal Couture, Dany Joly, Xavier Tastet, Vincent Aimez, Raynald Gauvin, CASINO V2.42—A fast and easy-to-use modeling tool for scanning electron microscopy and microanalysis users, Scanning 29 (3) (2007) 92–101, http://dx.doi.org/10.1002/sca.20000.

[18] Nanke Jiang, Daniel G. Georgiev, Ting Wen, Ahalapitiya H. Jayatissa, Reactive radio frequency sputtering deposition and characterization of zinc nitride and oxynitride thin films, Thin Solid Films 520 (6) (2012) 1698–1704, http://dx.doi.org/10.1016/j.tsf.2011.08.038.

[19] D.E. Partin, D.J. Williams, M. O'Keeffe, The crystal structures of Mg3N2 and Zn3N2, J. Solid State Chem. 132 (1) (1997) 56–59, http://dx.doi.org/10.1006/jssc.1997.7407.

[20] Haibo Gao, Xiaodan Zhang, Ying Zhao, Baojie Yan, The correlation of material properties and deposition condition of ZnON thin films, AIP Adv. 7 (2) (2017) 025111, http://dx.doi.org/10.1063/1.4977196.

[21] Nanke Jiang, Daniel G. Georgiev, Ahalapitiya H. Jayatissa, The effects of the pressure and the oxygen content of the sputtering gas on the structure and the properties of zinc oxy-nitride thin films deposited by reactive sputtering of zinc, Semicond. Sci. Technol. 28 (2) (2013) 025009, http://dx.doi.org/10.1088/0268-1242/28/2/025009.

[22] Haibo Gao, Xiaodan Zhang, Ying Zhao, Baojie Yan, Effect of process pressure and temperature on ZnON material properties in reactive sputtering, AIP Adv. 7 (3) (2017) 035311, http://dx.doi.org/10.1063/1.4978771.

[23] H McMurdie, M Morris, E Evans, B Paretzkin, W Wong-Ng, L Ettlinger, C Hubbard, ICDD powder diffraction, Powder Diffraction J. 1 (1) (1986) 76.

[24] Fenglin Xian, Jiandong Ye, Shulin Gu, Hark Hoe Tan, Chennupati Jagadish, Structural transition, subgap states, and carrier transport in anion-engineered zinc oxynitride nanocrystalline films, Appl. Phys. Lett. 109 (2) (2016) 023109, http://dx.doi.org/10.1063/1.4958294.

[25] A.R. Zanatta, Revisiting the optical bandgap of semiconductors and the proposal of a unified methodology to its determination, Sci. Rep. 9 (1) (2019) 11225, http://dx.doi.org/10.1038/s41598-019-47670-y.

[26] A. Dolgonos, T.O. Mason, K.R. Poeppelmeier, Direct optical band gap measurement in polycrystalline semiconductors: A critical look at the Tauc method, J. Solid State Chem. 240 (2016) 43–48, http://dx.doi.org/10.1016/j.jssc.2016.05.010.

[27] J. Tauc, R. Grigorovici, A. Vancu, Optical properties and electronic structure of amorphous germanium, Phys. Status Solidi b 15 (2) (1966) 627–637, http://dx.doi.org/10.1002/PSSB.19660150224.

[28] A. Ibrahim, S.K.J. Al-Ani, Models of optical absorption in amorphous semiconductors at the absorption edge — A review and re-evaluation, Czech. J. Phys. 44 (8) (1994) 785–797, http://dx.doi.org/10.1007/BF01700645.

[29] I. Hamberg, C.G. Granqvist, Evaporated Sn-doped In2O3 films: Basic optical properties and applications to energy-efficient windows, J. Appl. Phys. 60 (11) (1986) R123–R160, http://dx.doi.org/10.1063/1.337534.

[30] Mark Fox, Optical properties of solids, in: Oxford Master Series in Physics, second ed., Oxford University Press, 2010.

[31] S.M. Sze, K.K. Ng, Physics of Semiconductor Devices, John Wiley & Sons, Inc., Hoboken, NJ, USA, 2006, http://dx.doi.org/10.1002/0470068329.

[32] Jozeph Park, Yang Soo Kim, Kyung-Chul Ok, Yun Chang Park, Hyun You Kim, Jin-Seong Park, Hyun-Suk Kim, A study on the electron transport properties of ZnON semiconductors with respect to the relative anion content, Sci. Rep. 6 (1) (2016) 24787, http://dx.doi.org/10.1038/srep24787.
[33] D.K. Schroder, Semiconductor Material and Device Characterization, vol. 44, third ed., Wiley-IEEE Press, 2015, http://dx.doi.org/10.1063/1.2810086.
[34] V. Quemener, M. Alnes, L. Vines, P. Rauwel, O. Nilsen, H. Fjellvåg, E. V. Monakhov, B. G. Svensson, The work function of N-ZnO deduced from heterojunctions with Si prepared by ALD, J. Phys. D: Appl. Phys. 45 (31) (2012) 315101, http://dx.doi.org/10.1088/0022-3727/45/31/315101.